Hydrodynamic slip in silicon nanochannels

Bladimir Ramos-Alvarado,* Satish Kumar, and G. P. Peterson
The George W. Woodruff School of Mechanical Engineering, Georgia Institute of Technology, Atlanta, Georgia 30332, USA
(Received 13 January 2016; published 18 March 2016)

Equilibrium and nonequilibrium molecular dynamics simulations were performed to better understand the hydrodynamic behavior of water flowing through silicon nanochannels. The water-silicon interaction potential was calibrated by means of size-independent molecular dynamics simulations of silicon wettability. The wettability of silicon was found to be dependent on the strength of the water-silicon interaction and the structure of the underlying surface. As a result, the anisotropy was found to be an important factor in the wettability of these types of crystalline solids. Using this premise as a fundamental starting point, the hydrodynamic slip in nanoconfined water was characterized using both equilibrium and nonequilibrium calculations of the slip length under low shear rate operating conditions. As was the case for the wettability analysis, the hydrodynamic slip was found to be dependent on the wetted solid surface atomic structure. Additionally, the interfacial water liquid structure was the most significant parameter to describe the hydrodynamic boundary condition. The calibration of the water-silicon interaction potential performed by matching the experimental contact angle of silicon led to the verification of the no-slip condition, experimentally reported for silicon nanochannels at low shear rates.

DOI: 10.1103/PhysRevE.93.033117

I. INTRODUCTION

The robustness of the Navier-Stokes equations, i.e., the smallest possible dimension required to hold valid the definition of the shear viscosity, can be determined by means of a simple scale analysis [1]. For water, the smallest characteristic dimension was found to be $\sim$1 nm [1]. This result has been numerically verified through molecular dynamics (MD) simulations of water flowing through carbon nanotubes [2]. Alternatively, the no-slip boundary condition remains an empirical assumption, not presently supported by any physical principles [3]. While the no-slip boundary condition is usually applicable in macroscale systems, slip boundary conditions have been experimentally [4–6] and numerically [7–9] observed in nanoconfined flows.

Because of the limitations imposed by the dimensions of nanoscale flow systems for performing a reliable characterization of the boundary condition, MD simulations are commonly used to investigate the hydrodynamic behavior in nanochannels. Nonequilibrium MD (NEMD) simulations attempt to model shear-driven and body-force-driven flows. By profiling the velocity across the channels, the boundary condition is usually expressed as

$$u_s = L_s \left.\frac{\partial u}{\partial z}\right|_{z_0}, \tag{1}$$

where u_s is the slip velocity, $\partial u/\partial z$ is the velocity gradient evaluated at the solid-liquid interface z_0, and L_s is the parameter used to characterize the boundary condition, the hydrodynamic slip length. Here L_s can be determined as the length required to reach the no-slip boundary condition after performing a linear extrapolation of the velocity profile. Equilibrium MD (EMD) simulations can be used to obtain L_s by means of analyzing the fluctuation dissipation of the solid-liquid interaction forces. Equilibrium MD simulations pose advantages over NEMD in terms of avoiding the use of unphysical high shear rates (required to eliminate the noise in the calculations) and shorter simulation times. It has been demonstrated that EMD and NEMD calculations of L_s converge when the shear rate or driving force is small enough [10–12].

Currently, the true nature of L_s remains elusive and there are many parameters that can affect it. Previous investigations have reported that at small shear rates, L_s remains constant, but as the shear rate increases, different behaviors such as unbounded growth [13], bounded growth [14], and decay have been observed [15]. These different tendencies have been explained in terms of the type of liquid thermostat used [16] and/or the management of the excess heat induced in NEMD simulations [17]. A fundamental property affecting the behavior of the hydrodynamic slip is the wettability of the nanochannels surfaces. Wettability has been considered within a quasiuniversal relationship proposed to correlate L_s with the contact angle [18]. Huang *et al.* [18] and Sendner *et al.* [19] conducted a series of NEMD simulations of shear-driven nanochannel flow in which the wettability and roughness of different diamond surfaces were artificially modified. After performing scale analyses to analytical models of wettability and hydrodynamic slip, the expression $L_s \sim (1+\cos\theta)^{-2}$ was found, where θ is the contact angle. This expression was verified by coupling several MD simulations of wettability and nanochannel flow. Additionally, the scaling expression $L_s \sim \delta^4$ was proposed and verified, where δ is the liquid density depletion length given by

$$\delta = \int_0^\infty \left[1 - \frac{\rho_s(z)}{\rho_s^b} - \frac{\rho_l(z)}{\rho_l^b}\right] dz, \tag{2}$$

where $\rho_s(z)$ and $\rho_l(z)$ are the solid and liquid densities along the height of the nanochannel and ρ_s^b and ρ_l^b are the bulk solid and liquid densities, respectively.

Liu and Li [7] investigated the relationship between L_s and wettability by performing parametric analyses of the effect of the solid-liquid interaction potential on L_s. The contact angle corresponding to each interaction potential was not

*Corresponding author: bra3@gatech.edu

calculated in [7], but the results followed the trend suggested by the quasiuniversal relationship of L_s vs θ. However, the lack of calculation of θ poses a limitation to the practicality of this parametric analysis. Voronov *et al.* [13] performed a parametric study of the relationship between L_s and θ by independently varying the energy and length parameters of the solid-liquid nonbonded interaction potential. It was found that opposite trends with respect to the contact angle can be obtained, namely, L_s can increase as θ increases and L_s can decrease as θ increases, depending on the interaction potential parameter varied. More recently, Ho *et al.* [20] reported that slip can occur in a hydrophilic nanochannel if the solid-liquid affinity and the corrugation of the solid-liquid interaction potential allow the formation of liquid density bridges at the interface.

Silicon is a material of major importance for diverse technological applications, hence the importance and necessity of characterizing its interfacial properties in aqueous environments. The purpose of the current investigation is to obtain the relationship between L_s and θ for silicon nanochannels in which the wettability of the surfaces is artificially modified by changing the solid-liquid energy affinity. Two silicon planes in contact with water are investigated: the low-atomic-density Si(100) plane and the higher-density Si(111) plane. No artificial modification of the silicon structure was induced, thus allowing for the atomic planar density to affect the wettability and hydrodynamic slip. Equilibrium MD and NEMD simulations were carried out to obtain L_s.

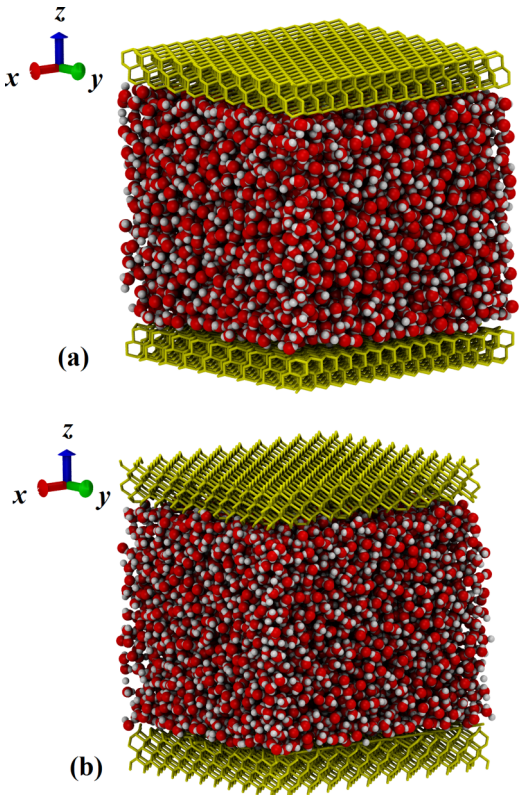

FIG. 2. (a) Si(111) and (b) Si(100) nanochannels.

II. WETTABILITY AND HYDRODYNAMIC SLIP CALCULATIONS

Equilibrium MD simulations of cylindrical water slabs were conducted to obtain θ for water on different silicon planes, Si(100) and Si(111), following the formalized methodology reported in [21]. In these simulations a water block was placed on top of a silicon surface at a prudent distance [Fig. 1(a)] and then allowed to equilibrate at constant temperature [Fig. 1(b)]. After equilibration, the atom coordinates were recorded at fixed time intervals and the density contours $\rho(x,z)$ were calculated by time averaging the liquid particles count per unit volume of the bins in which the x-z plane was divided. From the density contours, the bulk density of the liquid ρ_{bulk} was obtained by performing a sigmoidal function fit [22] of the density profile along the centerline of the droplet and finally the interface region was identified by the bins where $\rho(x,z) = \rho_{\text{bulk}}/2$ and then fitted with a circular function from which θ was calculated at the solid-liquid interface. The number of liquid molecules in the droplet was varied between 2000 and 8000 in order to ensure size-independent calculations of θ. For a more comprehensive description of the modeling procedures and postprocessing methodology, refer to [21,23].

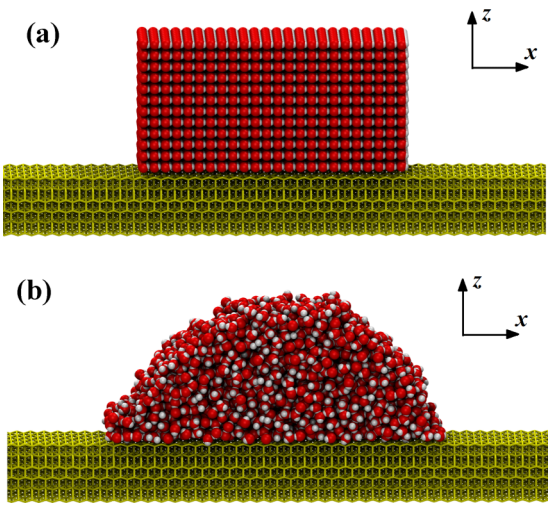

FIG. 1. Droplet wettability simulations steps: (a) initial configuration and (b) equilibrium droplet.

The nanochannels under investigation were formed by two silicon slabs confining a water block as shown in Fig 2. The confinement size was 5 nm, i.e., the distance between the innermost silicon atomic planes in the z direction. The area was $5.76 \times 5.98\ \text{nm}^2$ for Si(111) and $5.97 \times 5.97\ \text{nm}^2$ for Si(100). The equilibrium theory proposed by Huang and Szlufarska [24] was used to calculate the slip length as $L_s = \eta/\lambda(0)$, where η is the shear viscosity of water and $\lambda(0)$ is the zero-frequency friction coefficient given by

$$\lambda(\omega) = \frac{1}{2Ak_BT[1-\alpha(\omega)]} \sum_i \int_0^\infty dt \langle F_i(0)F_i(t)\rangle e^{j\omega t} \quad (3)$$

and

$$\alpha(\omega) = \frac{1}{2Ak_BT} \sum_i \int_0^\infty dt \langle F_i(0)u_i(t)\rangle e^{j\omega t}, \quad (4)$$

where F_i is the force on the liquid particle i due to the solid-liquid interactions, u_i is the x-velocity component of the liquid particle i, A is the area of the channel wall, k_B is the Boltzmann constant, and T is the absolute temperature. The functions $F_i(t)$ and $u_i(t)$ were obtained from the EMD simulations. The normalization of $2A$ was not originally indicated in [24], but is a necessary adjustment when calculating λ using all the particles within the confinement.

As for the NEMD simulations of the nanochannels hydrodynamics, a uniform force was applied to each water molecule, resembling a body-force-driven flow. The velocity profile was obtained by dividing the confinement into 80 bins of equal thickness in the z direction and using the area of the corresponding silicon channel. The number of liquid particles per unit volume of the bins was calculated and time-averaged in order to determine the liquid density profile and the particle count per bin was used to normalize the time-averaged sum of the velocities per bin. Afterward, L_s was determined using Eq. (1) where the MD-derived velocity profile was fitted with a second-order polynomial and u_s and $\partial u/\partial z$ were calculated at the solid-liquid interface from extrapolation of the polynomial fitting.

III. MOLECULAR DYNAMICS MODELING

The open source code LAMMPS [25] was used to perform the MD simulations of wettability and nanochannels hydrodynamics and the software VMD [26] for visualization. The extended simple point charge (SPC/E) water model [27] was used for modeling the water due to its good predicting capabilities and reduced complexity; in addition it allows for comparisons with other investigations. The rigidity of the SPC/E model was enforced by means of the SHAKE [28] algorithm and the long-range Coulombic interactions were treated with the PPPM [29] algorithm with an accuracy of 1×10^{-6}. The silicon-water interactions were modeled with a truncated Lennard-Jones potential taking into account only silicon-oxygen interactions, where the potential cutoff was 15 Å, $\sigma_{SiO} = 2.635$ Å, and ϵ_{SiO} was varied to induce different wettability conditions. The Tersoff [30] potential was used for modeling the Si-Si interactions in a many-body fashion. The time step for the integration of the equations of motion was 1 fs for all simulations.

The computational box for the droplet wettability simulations was periodic in all directions with x-y dimensions of 12 and 3 nm, respectively, and the z dimension was 10 nm, a distance required to ensure no interaction between the particles in neighbor periodic images. Initially, an energy minimization was carried out, followed by an equilibration in the canonical ensemble at a constant temperature of 300 K using the Nosé-Hoover thermostat [31,32] for 0.5 ns, and then a microcanonical ensemble run (*NVE*) for 0.5 ns to ensure that the system maintained a constant temperature in the absence of a thermostat. A production run of 3 ns (*NVE*) was used to sample the liquid water coordinates every 0.5 ps in order to calculate the contact angle from the geometry of the droplet as indicated in the previous section.

The number of liquid particles confined between the nanochannel walls was varied in order to make comparisons among systems with similar bulk densities and pressures, but

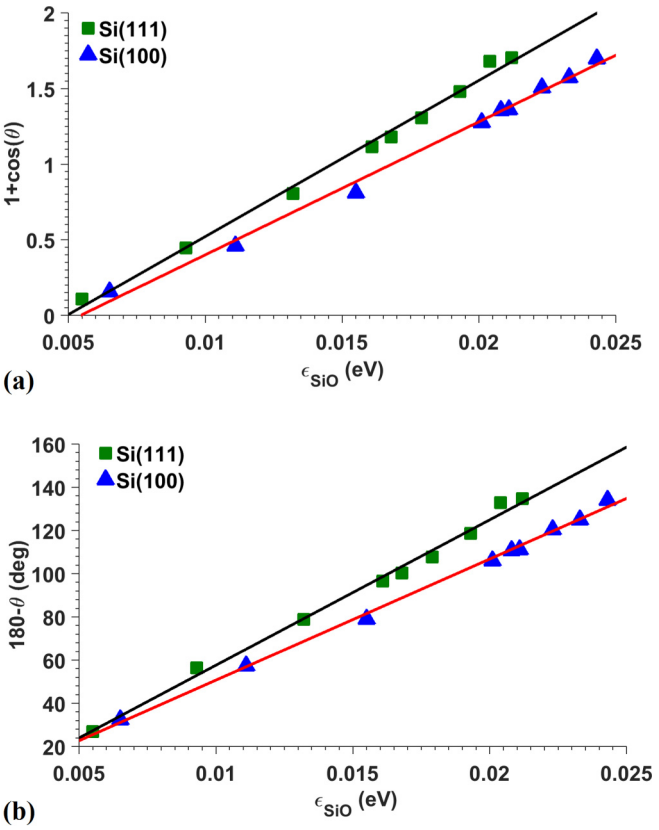

FIG. 3. Wettability of different silicon planes and the scaling laws correlating (a) $\epsilon \sim 1 + \cos(\theta)$ and (b) $\epsilon \sim 180^\circ - \theta$.

different surface wettabilities (see Sec. IV B). The simulations of EMD and NEMD hydrodynamics began with an energy minimization followed by an equilibration in the canonical ensemble with a thermal bath at 300 K for 1.5 ns. At this point two paths were taken. (i) In EMD, the water molecules coordinates and velocities were recorded every 10 fs for a total production time of 1 ns. These coordinates were used to rerun a simulation where only the solid-liquid interactions were considered to calculate F_i in Eq. (3). (ii) In NEMD, the thermostat of the water was removed and the equations of motion for water were integrated using pure Newtonian dynamics and at the same time an external force in the x direction was applied to every water molecule to induce flow for 1 ns. The solid atoms remained thermostated at 300 K using the Nosé-Hoover thermostat [31,32] to simulate natural cooling through the solid walls. A production run of 4 ns was used to sample the x component of the velocity of the water molecules and their coordinates every 0.5 ps.

IV. RESULTS AND DISCUSSION

A. Wettability of different silicon planes

The wettability of different silicon planes was characterized by the static contact angle calculated from the equilibrium geometry of cylindrical droplets. Size-independent results were achieved for droplets formed by 2300 water molecules and larger. The contact angles obtained are reported in Fig. 3 as a function of the energy potential parameter ϵ_{SiO},

which was used to artificially modify the wettability of the two silicon planes considered. Linear fits are depicted in each plot representing the scaling laws $\epsilon \sim 1 + \cos(\theta)$ and $\epsilon \sim 180^\circ - \theta$ proposed by Sendner *et al.* [19], in Figs. 3(a) and 3(b), respectively. As shown, the points corresponding to each silicon plane fit both of the scaling laws, but at the same time and as indicated in [19], it is difficult to discriminate which one is the most physically sound scaling law. Additionally, it is noteworthy that there is difficulty in sampling the hydrophobic region (small ϵ_{SiO}) where $\epsilon \sim 1 + \cos(\theta)$ loses accuracy; namely, a purely repulsive wall exists at a finite value of ϵ_{SiO}. It is important to note that these scaling laws are not universal, as the linear fittings are different for each silicon wetted plane. It can be formulated that the anisotropy of the silicon crystal (atomic planar density and atomic interlayer distance) has a significant effect on the wettability of this material.

Figures 3(a) and 3(b) clearly indicate that although the silicon atoms and water molecules interact through the same energy potential, Si(100) is consistently more hydrophobic than Si(111). This can be explained by the different planar atomic densities for these two planes. The Si(111) plane is denser, hence, the interaction force per unit area is larger than that for the low-density Si(100) surface. In addition, the underlying Si(111) structure is more closely packed due to its characteristic atomic triple bilayer periodic structure. These results were analyzed in Ref. [23], where a mean-field-theory-based model of wettability was used to describe the contact angles obtained from the MD simulations. The theory and simulation results showed good correlation confirming the intricate relationship among the interfacial liquid density, solid atomic planar density, and underlying solid structure anisotropy, with the contact angle. The scaling laws presented here are simple approximations, but should be considered as they constitute the origin of the slip-wettability scaling laws.

B. Nanoconfined water with similar bulk properties

The wettability of the nanochannels walls was varied as indicated in the previous section, hence producing a change in the minimum pressure P_0 required to push a liquid into a slitlike pore [33] of width h given by

$$P_0 = \frac{2(\gamma_{LS} - \gamma_{SV})}{h} = -\frac{2\gamma_{LV}\cos(\theta)}{h}, \tag{5}$$

where γ is the surface tension and LS, SV, and LV stand for liquid-solid, solid-vapor, and liquid-vapor, respectively. From a molecular point of view, Eq. (5) indicates that in order to achieve similar bulk properties, the number of liquid particles within the confinement needs to be adjusted (pressure is proportional to the number of particles at constant volume). The number of water molecules confined within 5 nm was varied from 5668 to 5776 to cover the range from hydrophobic to hydrophilic conditions, respectively. Figure 4 depicts the density profiles along the nanochannels height (z direction) for two wettability conditions of the walls, Fig. 4(a) hydrophilic and Fig. 4(b) hydrophobic, for both silicon structures. Similar bulk densities are observed in each case as well as a noticeable liquid layering for hydrophilic surfaces and a weak layering for hydrophobic surfaces, a typical characteristic. It is also noticeable that the Si(100) surface features a larger liquid density depletion and this is due to the low atomic density of the Si(100) plane.

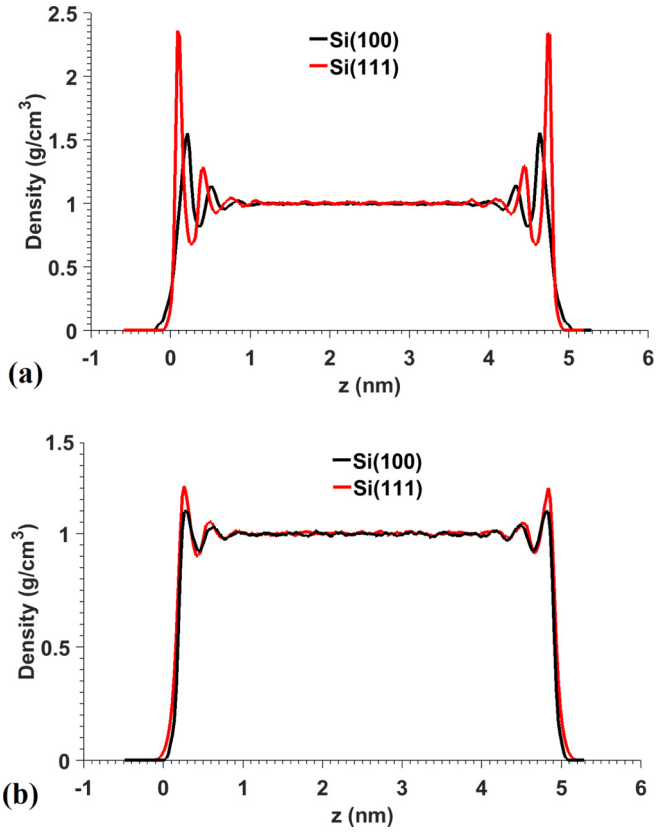

FIG. 4. Density profiles along the nanochannels height with contact angles of (a) $\theta = 71^\circ$ and (b) $\theta = 150^\circ$.

A major objective of the current investigation was to ensure that similar bulk properties were observed in every system, while varying the wettability of the nanochannels. This is important, since the hydrodynamic slip is an interfacial phenomenon. The density profiles have been highlighted, but it is important to note that similar bulk pressures were observed in a previous work [34]. The pressure oscillated around 0 bars with a range of variation between −200 and 200 bars in the bulk.

C. Hydrodynamic slip in silicon nanochannels under different wettability conditions

Equilibrium calculations of the friction coefficient $\lambda(0)$ were performed using the data derived from the EMD simulations and Eqs. (3) and (4). The hydrodynamic slippage was evaluated as $L_s = \eta/\lambda(0)$, where $\eta = 0.729 \times 10^{-3}$ Pa s is the shear viscosity of SPC/E water [35]. A nonbiased time-correlation algorithm was used for evaluating the correlation functions in Eqs. (3) and (4). The lag time for the evaluation of the autocorrelation function [upper limit of Eqs. (3) and (4)] was varied until observing saturation of λ at a value independent of the lag time. A sample of these calculations can be found in [34]. Eventually, a lag time of 40 ps was used for sampling the data and a time interval of 1 ps was used between consecutive evaluations of several time-correlation functions

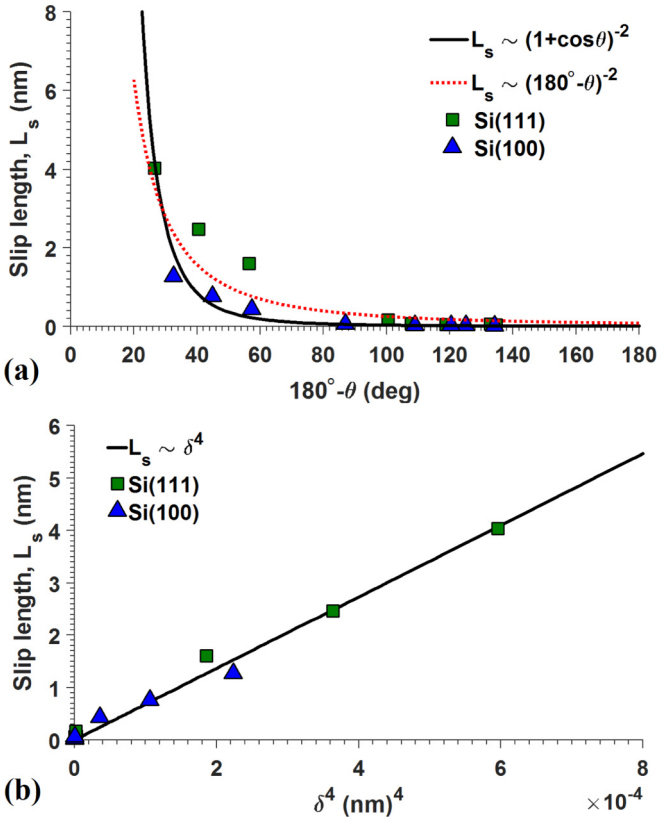

FIG. 5. Scaling laws of hydrodynamic slip: (a) slip length versus contact angle and (b) slip length versus depletion length.

for a time interval of 1 ns. The results are depicted in Fig. 5 as the average of three independent simulation sets.

The first objective of this investigation was to verify the quasiuniversal relation between wettability and hydrodynamic slippage proposed by Sendner *et al.* [19]. Figure 5(a) illustrates L_s as a function θ, both obtained from EMD simulations for Si(111) and Si(100) nanochannels. It was observed that for $\theta < 100^\circ$, L_s is practically zero for both silicon surfaces and therefore is similar. However, for $\theta > 100^\circ$, noticeable differences begin to arise. Also, L_s is consistently greater in Si(111) than in Si(100) nanochannels. This is understandable, since the Si(111) plane offers a smoother surface to the liquid particles than the rougher (lower planar atomic density) Si(100). The roughness effect at the nanoscale is essentially a corrugation of the solid-liquid interaction potential. Figure 5(a) depicts the two scaling laws reported in [19] to correlate L_s and θ. These curves were obtained by a nonlinear least-squares algorithm using as input data for both silicon nanochannels. Although both laws seem to somehow predict the tendencies observed, it is clear that independent fittings for each silicon nanochannel would lead to a better match with MD simulations. These results raise a concern on the universality of the scaling laws, since L_s is affected by θ and the granularity of the solid structure of each individual nanochannel.

Figure 5(b) illustrates the relationship between hydrodynamic slippage and the liquid density depletion caused by different solid-liquid affinity conditions. The depletion length δ was calculated using Eq. (2), where the upper limit of the integral was defined as half of the height of the nanochannels ($z = 2.5$ nm). The scaling law $L_s \sim \delta^4$ illustrated in Fig. 5(b) represents a remarkable improvement upon the previous scaling laws based on wettability. A single curve matches the hydrodynamic slippage reported in different silicon nanochannels under a wide range of wettability conditions. Since δ is a function of the solid-liquid affinity, given by ϵ_{SiO} (interaction potential), and the liquid density depletion caused by liquid entrainment in the corrugations of the solid-liquid interaction potential (planar atomic density and solid structure), it poses a better alternative than θ to predict hydrodynamic slippage. This is understandable, since the level of density depletion is directly correlated with the effectiveness of the momentum exchange between the solid and liquid phases. Alternatively, the contact angle obtained from MD simulations consists of a calibration process. Although θ is correlated with δ, the MD simulations of droplets wettability can be calibrated to obtain any contact angle by modifying one of two interaction potential parameters.

Nonequilibrium MD simulations of body-force driven flow were conducted in Si(111) and Si(100) nanochannels under different wettability conditions. Unlike EMD, NEMD simulations are strongly affected by the noisiness of the calculations of the velocity profiles (statistical noise due to binning) in a single simulation and variations obtained between independent simulations. The velocity profiles obtained via NEMD are depicted in Fig. 6 for Si(111) and Si(100) nanochannels under hydrophilic and hydrophobic conditions. Forces varying between 1×10^{-5} and 8×10^{-5} eV/Å were

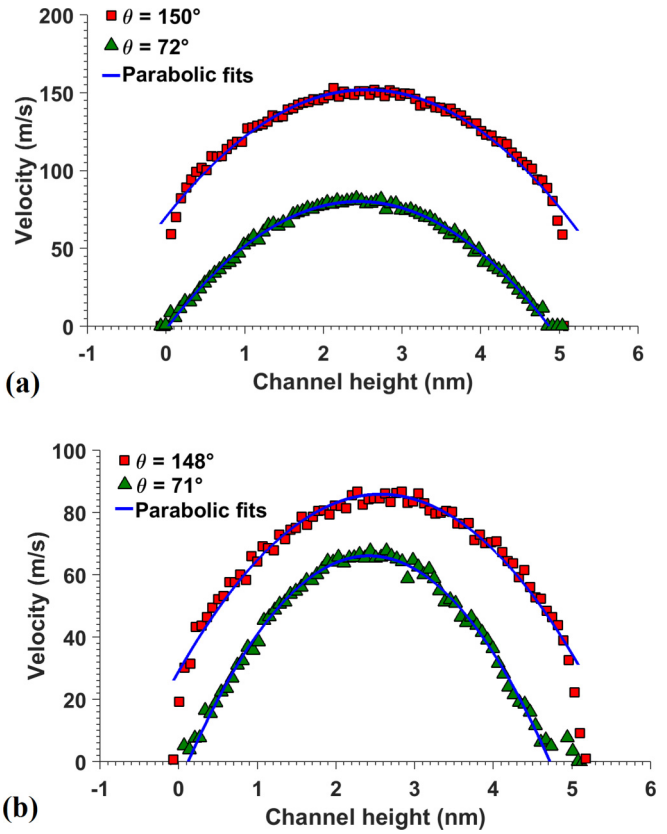

FIG. 6. Nonequilibrium velocity profiles for (a) Si(111) and (b) Si(100) nanochannels.

applied to each water molecule for the hydrophilic and hydrophobic cases in order to identify the low-shear-rate limit for a proper comparison between NEMD and EMD simulations. Figures 6(a) and 6(b) depict a consistency with the EMD calculations, i.e., no slip, for Si(111) and Si(100) nanochannels for the given hydrophilic condition. For hydrophobic Si(100) nanochannels $L_s = 0.9 \pm 0.24$ nm was obtained from the NEMD calculations, a value consistent with the average 1.28 nm obtained from EMD. Alternatively, the hydrophobic Si(111) nanochannel featured a more noticeable discrepancy between the methods for calculating slip. In the limit of low shear rate, $L_s = 1.8 \pm 0.83$ nm was calculated for hydrophobic Si(111). The larger margin of error arises from the noisiness of the calculations when the gradients imposed are too small, which was necessary for this nanochannel. A factor of 2 is observed in the difference between the NEMD and EMD calculations for this particular condition. Discrepancies between EMD and NEMD simulations of hydrodynamic slippage have been previously reported [10,11,24] as there is still a lack of consensus on the accuracy of the equilibrium theories for the calculation of hydrodynamic slip [34].

The accurate measurement of interfacial or bulk properties strongly depends on the resolution of the instruments, which is a major issue at these small length scales. In the field of nanofluidics, a tendency toward reduction of the slip length measurements has been observed as the resolution of the measuring techniques increases [1]. The principal methods for performing slip length measurements in nanoconfined liquids use the surface force apparatus, atomic force microscopy, and microparticle image velocimetry [1]; however, some other techniques have been applied successfully. Recently, Li *et al.* [36] experimentally investigated the flow dynamics in a silicon nanochannels array, where each nanochannel had a cross section of 100 nm $\times$ 100 μm. By varying the flow rate and recording the pressure drop of the array, the shear rate was determined from an analytical model taking into account the hydrodynamic slip. From the data fitting, it was observed that there was no slip until a shear rate of $1 \times 10^5\ \mathrm{s}^{-1}$ was reached. This experimental observation is consistent with the calculations presented here for silicon nanochannels using EMD and NEMD calculations at low-shear-rate conditions. The wettability of pristine silicon is difficult to measure, but recent experiments have determined that the contact angle for water on silicon is $\sim 77^\circ$ [37], a value included in the range of hydrophilic conditions investigated herein. Thus, by calibrating the silicon-water interaction potential to a contact angle of 77°, it was possible to obtain the no-slip boundary condition at low shear rates as reported from experiments [36].

D. Interfacial liquid structure under different wettability conditions

The wettability of the nanochannels walls was shown to be a useful parameter in the determination of the slippage in nanoconfined liquids; however, it is not as significant as the interfacial liquid structure properties (affected by the solid structure and solid-liquid interaction strength) (see Fig. 5). Thus, the granularity of the solid-liquid interaction potential plays an important role in the hydrodynamics of nanoconfined flows, as it affects the level of water particles entrainment and hence the solid-liquid momentum transfer (affecting the type of boundary condition). The density contours of a liquid slab 1 Å thick, positioned at the first liquid layer, the highest-density peak observed in Fig. 4 for each condition, were obtained to visualize the two-dimensional liquid structure under hydrophilic [$\theta = 72^\circ$ for Si(111) and $\theta = 71^\circ$ for Si(100)] and hydrophobic conditions [$\theta = 150^\circ$ for Si(111) and $\theta = 148^\circ$ for Si(100)]. Figure 7 illustrates the density contours under hydrophilic conditions for Si(111) and Si(100) nanochannels. Under the strong solid-liquid affinity conditions depicted in Fig. 7(a), it is observed that the hexagonlike pattern of the Si(111) plane is imprinted onto the first atomic liquid layer. Likewise, the large interstitial spaces between the atoms of the Si(100) plane in the [111] direction form a potential well where liquid particles get trapped. It is apparent here that

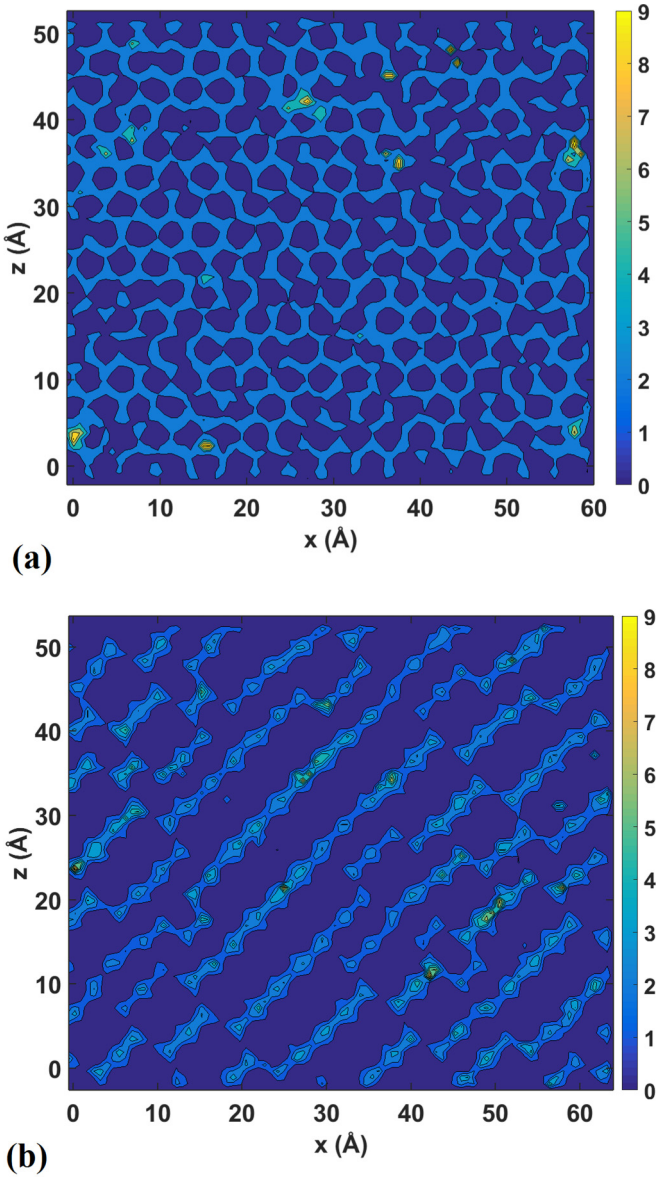

FIG. 7. Interfacial density contours (g/cm^3) under hydrophilic conditions for (a) Si(111) and (b) Si(100) nanochannels. The low-density regions at the ends of the z direction are only visual artifacts of the postprocessing stage.

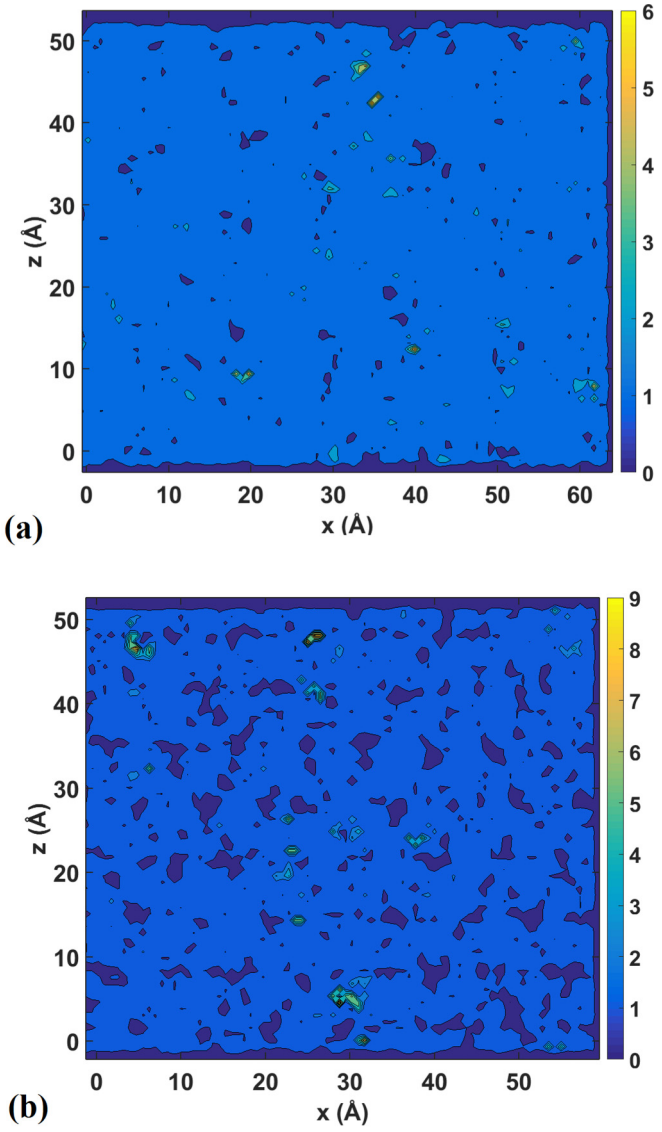

FIG. 8. Interfacial density contours (g/cm^3) under hydrophobic conditions for (a) Si(111) and (b) Si(100) nanochannels. The low-density regions at the ends of the z direction are only visual artifacts of the postprocessing stage.

under strong solid-liquid affinity conditions, the granularity of the solid surfaces is imprinted on the interfacial water, thus promoting a no-slip hydrodynamic condition. These observations add to the understanding of the no-slip boundary condition in Si(111) and Si(100) from the perspective of the interfacial liquid structure parallel to the walls, while the density depletion length provides information about the water structure in the direction normal to the walls. Interestingly, Ho *et al.* [20] indicated that interfacial structures like the ones depicted in Fig. 7 represent density bridges, meaning that liquid particles can move throughout the interface causing slippage to occur. However, the results reported herein indicate that these connected interfacial structures represent a rather strong solid-liquid attraction that decreases or eliminates slip by reducing the depletion length.

When the solid-liquid affinity is weak, such as in the case of hydrophobic conditions (see Fig. 8), the interfacial liquid structure parallel to the wall surface is characterized by smooth density contours. Compared with the density contours of Fig. 7, the granularity of the solid surface is no longer imprinted on the interfacial liquid structure. This indicates a less effective momentum transfer between the solid and liquid particles. Additionally, the uniform density contours observed in Figs. 8(a) and 8(b) reveal the presence of a smooth barrier created by the repulsive contribution of the solid-liquid interaction potential, above which the liquid particles are prone to slip due to the weak attraction and the smoothness of the energy landscape. Finally, these uniform density contours and the smooth energy barrier that leads to create them help to explain the differences in the hydrodynamic slip observed between Si(100) and Si(111) for similar contact angles, i.e., in order to observe the same contact angle between these two different silicon surfaces, the Si(100)-water interaction potential is stronger than for Si(111) in order to compensate for the lower atomic planar density of the Si(100) surface; hence, L_s is smaller for Si(100).

V. CONCLUSION

Equilibrium and nonequilibrium molecular dynamics simulations were conducted to investigate the hydrodynamic slip in Si(111) and Si(100) nanochannels. The starting point of the current investigation was to determine the wettability of the Si(111) and Si(100) surface by means of equilibrium simulations of droplets wettability. The size-independent calculations of the contact angle on the different silicon surfaces revealed that not only the solid-liquid interaction strength, but also the underlying liquid structure plays a major role in the calculation of the contact angle. Equilibrium simulations and the theory proposed by Huang and Szlufarsza [24] were used to correlate the hydrodynamic slip length with the contact angle measured on different silicon surfaces. The obtained results followed the quasiuniversal relationship proposed by Sendner *et al.* [19], but with a noticeable difference between the different silicon nanochannel structures. An improved correlation was obtained between hydrodynamic slippage and the depletion length, also suggested in [19]. By considering the interfacial liquid structure and planar atomic density, the depletion length poses a better alternative to predict and correlate the hydrodynamic slip length in a more universal fashion. These observations were supported by nonequilibrium simulations of flow in the nanochannels investigated and by observing the interfacial liquid structure changes produced under hydrophilic and hydrophobic conditions. In addition, by calibrating the silicon-water interaction potentials to obtain the experimental contact angle of 77° for silicon, it was possible to determine that a no-slip condition exists at low shear rates as was recently determined from experiments with silicon nanochannels.

ACKNOWLEDGMENTS

B.R.-A. was partially supported by the Mexican Council on Science and Technology under Scholarship No. 312756.

[1] L. Bocquet and E. Charlaix, Chem. Soc. Rev. **39**, 1073 (2010).
[2] J. A. Thomas and A. J. H. McGaughey, Phys. Rev. Lett. **102**, 184502 (2009).
[3] D. C. Tretheway and C. D. Meinhart, Phys. Fluids **14**, L9 (2002).
[4] D. Lasne, A. Maali, Y. Amarouchene, L. Cognet, B. Lounis, and H. Kellay, Phys. Rev. Lett. **100**, 214502 (2008).
[5] D. Schaeffel, S. Yordanov, M. Schmelzeisen, T. Yamamoto, M. Kappl, R. Schmitz, B. Dünweg, H.-J. Butt, and K. Koynov, Phys. Rev. E **87**, 051001(R) (2013).
[6] O. I. Vinogradova, K. Koynov, A. Best, and F. Feuillebois, Phys. Rev. Lett. **102**, 118302 (2009).
[7] C. Liu and Z. Li, Phys. Rev. E **80**, 036302 (2009).
[8] C. Liu and Z. Li, AIP Adv. **1**, 032108 (2011).
[9] H. Zhang, Z. Zhang, Y. Zheng, and H. Ye, Phys. Rev. E **81**, 066303 (2010).
[10] S. K. Kannam, B. D. Todd, J. S. Hansen, and P. J. Daivis, J. Chem. Phys. **135**, 144701 (2011).
[11] Z. Liang and P. Keblinski, J. Chem. Phys. **142**, 134701 (2015).
[12] N. Wei, X. Peng, and Z. Xu, Phys. Rev. E **89**, 012113 (2014).
[13] R. S. Voronov, D. V. Papavassiliou, and L. L. Lee, J. Chem. Phys. **124**, 204701 (2006).
[14] A. Martini, H. Y. Hsu, N. A. Patankar, and S. Lichter, Phys. Rev. Lett. **100**, 206001 (2008).
[15] A. Alizadeh Pahlavan and J. B. Freund, Phys. Rev. E **83**, 021602 (2011).
[16] S. Bernardi, B. D. Todd, and D. J. Searles, J. Chem. Phys. **132**, 244706 (2010).
[17] S. De Luca, B. D. Todd, J. S. Hansen, and P. J. Daivis, J. Chem. Phys. **140**, 054502 (2014).
[18] D. M. Huang, C. Sendner, D. Horinek, R. R. Netz, and L. Bocquet, Phys. Rev. Lett. **101**, 226101 (2008).
[19] C. Sendner, D. Horinek, L. Bocquet, and R. R. Netz, Langmuir **25**, 10768 (2009).
[20] T. A. Ho, D. V. Papavassiliou, L. L. Lee, and A. Striolo, Proc. Natl. Acad. Sci. USA **108**, 16170 (2011).
[21] B. Ramos-Alvarado, S. Kumar, and G. P. Peterson, J. Chem. Phys. **143**, 044703 (2015).
[22] M. J. de Ruijter, T. D. Blake, and J. De Coninck, Langmuir **15**, 7836 (1999).
[23] B. Ramos-Alvarado, S. Kumar, and G. P. Peterson, J. Chem. Phys. **144**, 014701 (2016).
[24] K. Huang and I. Szlufarska, Phys. Rev. E **89**, 032119 (2014).
[25] S. Plimpton, J. Comput. Phys. **117**, 1 (1995).
[26] W. Humphrey, A. Dalke, and K. Schulten, J. Mol. Graphics Model. **14**, 33 (1996).
[27] H. J. C. Berendsen, J. R. Grigera, and T. P. Straatsma, J. Phys. Chem. **91**, 6269 (1987).
[28] J.-P. Ryckaert, G. Ciccotti, and H. J. Berendsen, J. Comput. Phys. **23**, 327 (1977).
[29] R. W. Hockney and J. W. Eastwood, *Computer Simulation Using Particles* (Hilger, Bristol, 1988), p. xxi.
[30] J. Tersoff, Phys. Rev. B **38**, 9902 (1988).
[31] S. Nosé, Mol. Phys. **52**, 255 (1984).
[32] W. G. Hoover, Phys. Rev. A **31**, 1695 (1985).
[33] J. L. Barrat and L. Bocquet, Faraday Discuss. **112**, 119 (1999).
[34] B. Ramos-Alvarado, S. Kumar, and G. P. Peterson, Phys. Rev. E **93**, 023101 (2016).
[35] M. A. Gonzalez and J. L. F. Abascal, J. Chem. Phys. **132**, 096101 (2010).
[36] L. Li, J. Mo, and Z. Li, Phys. Rev. E **90**, 033003 (2014).
[37] A. Egatz-Gomez, R. Majithia, C. Levert, and K. E. Meissner, RSC Adv. **2**, 11472 (2012).